A&A 476, 63–72 (2007)
DOI: 10.1051/0004-6361:20077966

Astronomy
&
Astrophysics

# The distant galaxy cluster CL0016+16: X-ray analysis up to $R_{200}$

L. Solovyeva, S. Anokhin, J. L. Sauvageot, R. Teyssier, and D. Neumann

CEA/DSM/DAPNIA, Service d'Astrophysique, L'Orme des Merisiers, Bât. 709, 91191 Gif-sur-Yvette, France
e-mail: `lilia.solovyeva@cea.fr`

Received 29 May 2007 / Accepted 11 September 2007

## ABSTRACT

*Aims.* CL0016+16 seems to be a good candidate for studying the mass distribution of galaxy clusters up to their Virial radius, since it is a bright massive cluster, previously considered as dynamically relaxed.
*Methods.* Using XMM-Newton observations of CL0016+16, we performed a careful X-ray background analysis and detected its X-ray emission convincingly up to $R_{200}$. We then studied its dynamical state with a detailed 2D temperature and surface brightness analysis of the inner part of the cluster. We used the assumption of both spherical symmetry and hydrostatic equilibrium (HE), to determine the main cluster parameters: total mass, temperature profile, surface brightness profile, and $\beta$-parameter. We also built a temperature map that clearly exhibits departure from spherical symmetry in the centre. To estimate the influence of these perturbations on our total mass estimate, we also computed the total mass in the framework of the HE approach, but this time with various temperature profiles obtained in different directions.
*Results.* These various total-mass estimates are consistent with each other. The temperature perturbations are clear signatures of ongoing merger activity. We also find significant residuals after subtracting the emissivity map by a 2D $\beta$-model fit. We conclude that, although CL0016+16 shows clear signs of merger activity and departure from spherical symmetry in the centre, its X-ray emissivity can be detected up to $R_{200}$ and the corresponding mass $M_{200}$ can be computed directly. It is therefore a good candidate for studying cosmological scaling laws as predicted by the theory.

**Key words.** X-rays: galaxies: clusters – X-rays: individuals: CL0016+16

## 1. Introduction

In the hierarchical scenario of structure formation, clusters of galaxies are the largest and youngest *virialised* objects in the Universe. This makes them ideal targets for cosmological studies. Clusters of galaxies are self-similar in shape, and the cluster population obeys scaling laws for various physical properties: total mass, temperature, and luminosity. The evolution of these properties with redshift gives also complementary information that shed light on cluster physics. The X-ray observations of galaxy clusters allow us to study the hot intracluster medium (ICM), which is the main baryon reservoir in galaxy clusters. In the era of XMM-Newton and Chandra observations, we can obtain detailed information on the density and temperature distribution of the ICM, and study their internal structure with unprecedented accuracy.

This paper reports a detailed study of CL0016+16, a very massive, luminous, and distant ($z = 0.54$) galaxy cluster. CL0016+16 is one of the most extensively studied clusters of galaxies in different wavelengths, in particular in the optical (Tanaka et al. 2005), radio (Giovannini & Feretti 2000) bands and for Sunyaev-Zel'dovich effect (Birkinshaw et al. 1981; Bonamente et al. 2006). It has been also studied using weak lensing (Clowe et al. 2000) and X-rays from ROSAT (Neumann & Bohringer 1997) and XMM-Newton (Kotov & Vikhlinin 2005; Worrall & Birkinshaw 2003).

The question about the dynamical state of this cluster is still open. Previous X-ray analysis has concluded that the cluster might be relaxed (Kotov & Vikhlinin 2005). But we know that this cluster has a radio halo from Giovannini & Feretti (2000), which can be a signature of merger activity. Since the total mass is computed using the hydrostatic equilibrium approach, we need to have a better idea of the dynamical state of the cluster.

In this paper, we present a detailed spectro-imaging study of the galaxy cluster CL0016+16. We first assumed that the cluster is relaxed and spherically symmetric. We obtained highquality surface brightness profiles using different background subtraction methods and demonstrated that we can detect the cluster emission up to $R_{200}$. This specific radius was first used by theoreticians to define dark matter halos, for which the mean density is 200 times the critical density of the universe. An $N$ body and hydrodynamics numerical simulations have shown that, within this radius, the gas and dark matter halo can be reasonably considered to be in dynamical equilibrium (Cole & Lacey 1996). To compute $R_{200}$, we use the standard definition:

$$M_{200} = \frac{4\pi}{3} 200 \rho_{\mathrm{crit}}(z) R_{200}^3 \tag{1}$$

where $\rho_{\mathrm{crit}} = 3H_0^2/8\pi G$ is the critical density, and our cosmological parameters $\Omega_{\mathrm{m}} = 0.3$, $\Omega_\Lambda = 0.7$, and $H_0 = 70\ \mathrm{km\ s^{-1}\ Mpc^{-1}}$. Most theoretical predictions (mass function, density profiles, scaling laws) are computed within this radius, while most X-ray observations are limited to much more inner regions, such as $R_{1000}$.

The purpose of this paper is to compute the observed properties of a large X-ray cluster within $R_{200}$. Using the hydrostatic equilibrium and first guesses of the $\beta$-model parameters and mean temperature of 8.9 keV taken from Kotov & Vikhlinin (2005), we used Eq. (1) to estimate that $R_{200} = 1.92$ Mpc or 5′

for $z = 0.54$. We then verified that our measurement of temperature at $R_{200}$ is very similar to the used value. In a second step, we performed a detailed spectral analysis of CL0016+16, and deduced its average temperature, its temperature profile, and a highquality temperature map. To estimate the influence of temperature variations on the total mass estimate, we calculated the mass profile using the hydrostatic equilibrium equation and different temperature profiles in different directions. Finally, using the $\Lambda CDM$ cosmological model, we tested how CL0016+16 fits into the cosmological self-similarity theory. All errors on the cluster parameters were obtained at the 68% confidence level.

## 2. Data analysis

We studied the physical parameters and ICM dynamics of CL0016+16 up to $R_{200}$. The cluster emission is weak in the external region, so the astrophysical background can play the main role in the outer region. This is why the treatment of background is very important. To obtain the best result we used three different backgrounds for subtraction in the data analysis. These were the background of A. Read without "flare" rejection, the background of J. Nevalainen with "flare" rejection, and the modelling of background using the observation data.

The method of double background subtraction from Arnaud et al. (2002b) was used. For analysis we used the XMM- Newton data from EPIC cameras (MOS 1, 2 and pn) and the XMM-Newton Science Analysis System (SAS) for data reduction. In the MOS 1, 2 data set we took into account event patterns 0 to 12 and in pn data - patterns 0 to 4, flag = 0. The sky coordinates of background observation in the event files were modified using the aspect solution of CL0016+16 observation. From the count rate of the observation data we detected and excluded the periods of "flare". We used the count rate of the observation in the high energy bands (10–12 keV) and exposure time of the observation to normalise the background.

The effective area of the XMM-Newton mirrors is a function of the off-axis angle and energy of the photons. One could manage it through a weight function directly computed for each event (Majerowicz et al. 2002) or through an exposure map. The vignetting is a geometrical effect, and both approaches lead to similar results. Throughout this work we have used the weight method.

We excluded all detectable point sources from the data observation in our spectral and spatial analysis. The sources were detected in the 0.3–4.5 keV energy bands. Detected point sources were masked with circles of 70% point-spread-function power radii.

### 2.1. Double subtraction

After cleaning the flare events, the XMM background is dominated by the cosmic X-ray background (CXB) and non X-ray background (NXB) induced by high-energy particles. Our analysis used the double-subtraction method by Arnaud et al. (2002b) for background subtraction.

The background subtraction for profile and spectrum consists of two steps. Firstly, we subtract the normalised blank field obtained using the same spatial and energy selection (NXB component), and then subtract the residual components using the data in the outer part of the cluster emission (CXB component).

### 2.2. Background subtraction (blank field of A. Read)

The background of A. Read is a blank field without any "flare" rejection (Read & Ponman 2003). We excluded the "flare" period using a similar method for the observation and background. We suggested that the residual "flare" background could play a role in each energy band. That is why we performed the "flare" rejection in the standard selection for the observation and background data (Majerowicz et al. 2002) and for each energy band (10–12 keV, 0.3–12 keV, 2–5 keV, 0.3–2 keV). To determine the best limit of "flare" background, we used the light curve and compared the histograms obtained from the images in the external regions. Using different energy bands for the "flare" rejection, we obtained the same results and the same exposure times.

### 2.3. Background subtraction (blank field of J. Nevalainen)

To obtain the best result from the image analysis so as to detect the cluster emission up to $R_{200}$ with the XMM-Newton data, we also performed the image analysis with the background of Nevalainen (Nevalainen et al. 2005). The background data of Nevalainen is cleaned for "flares", has better statistic and less sources and no artefacts in the centre of the FOV. In this analysis for observation we excluded the "flare" rejection in the standard selection with the Poisson filter the flares were detected as $>3\sigma$ deviation from the mean.

## 3. Image analysis

### 3.1. Surface brightness profile

The surface brightness profile was fitted with the $\beta$-model (Cavaliere & Fusco-Femiano 1976) in which the surface brightness $S(r)$ is defined as

$$S(r) = S_0 \left(1 + \frac{r^2}{r_c^2}\right)^{-3\beta+0.5} \tag{2}$$

where $S_0$ is the central intensity, $r_c$ – the core radius, $\beta$ – the slope parameter. The best-fit $\beta$-model was used to compute the total mass. The $\beta$-model allows us to project the surface brightness of the ICM easily. It emits via thermal bremsstrahlung into the following gas density profile:

$$n(r) = n_0 \left(1 + \frac{r^2}{r_c^2}\right)^{-3\beta/2} . \tag{3}$$

#### 3.1.1. Surface brightness profile with the blank field of A. Read

To obtain the surface brightness profile using the background of A. Read, we created the images in the 0.3–4.5 keV and calculated the corresponding exposure maps taking into account the detector geometry for the observation and background data for the XMM-Newton three cameras. The radial surface brightness profiles were created from these images and three profiles were summed. Significant cluster emission was detected up to $R_{200}$ with a detection limit of $3\sigma$. The $\beta$-fits of cluster profile are given in the Table 1, and the convolved best fit $\beta$-model is plotted in Fig. 1a.

#### 3.1.2. Surface brightness profile with the blank field of J. Nevalainen

To obtain a surface brightness profile using background from Nevalainen, we extracted the surface brightness profile of the

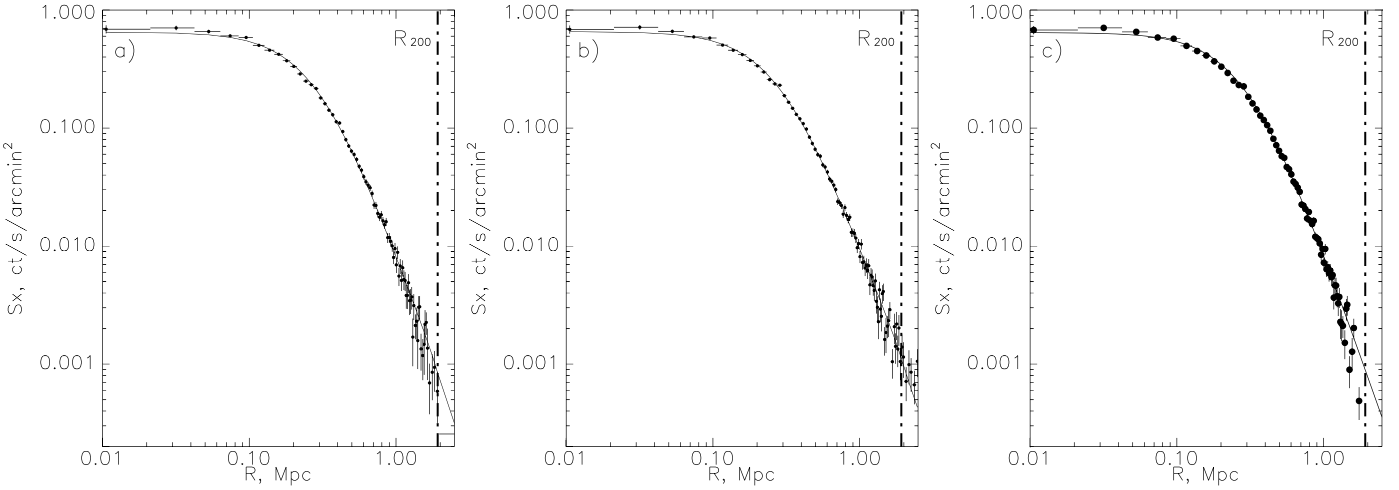

**Fig. 1.** The surface brightness profiles combined MOS1, MOS2, and pn cameras obtained using different backgrounds: **a)** the background of A. Read, **b)** the background of Nevalainen, and **c)** the background model from observation data. The solid line is the best-fit $\beta$-model.

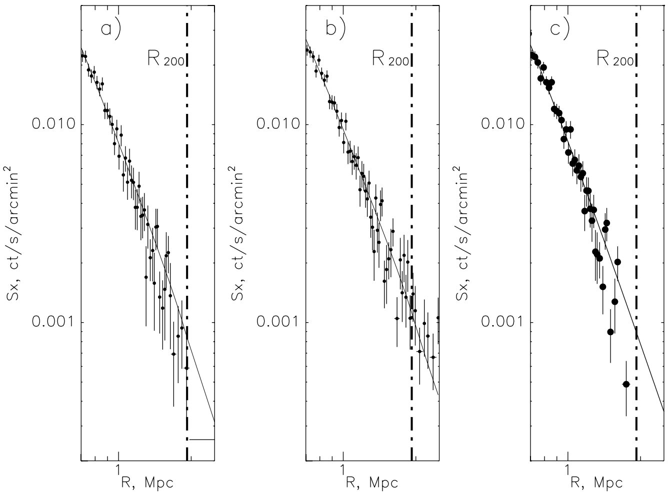

**Fig. 2.** The combined (MOS1, MOS2, pn) surface brightness profiles in the external region obtained using: **a)** the background of A. Read, **b)** the background of J. Nevalainen, **c)** the background modelling from corresponding observation data. The solid line is the best-fit $\beta$-model.

cluster in the 0.3–4.5 keV energy band. This band was chosen to optimise the signal-to-noise ratio. We binned the photons into concentric annuli with a size of $1.65''$ centred on the maximum of the X-ray emission for each camera. The three profiles were then summed. The resulting surface brightness profile $S_0$ is shown in Fig. 1b. The cluster emission is clearly detected up to $R_{200}$, with a detection limit of $3\sigma$. We fitted $S_0$ with a $\beta$-model, without the first three points but with the PSF deconvolution (see the results in Table 1). The same results of the $\beta$-model fit parameters were obtained using all the points for the fits, $\beta = (0.73 \pm 0.02)$ and $r_c = (0.27 \pm 0.02)$ Mpc. This result is in a good agreement with those in Kotov & Vikhlinin (2005).

### 3.1.3. Surface brightness profile using the modelling of background from observation data

The astrophysical background plays a very important role in the data analysis of the outskirts of galaxy clusters, so we assumed that it would be better to use the observation data for the background modelling. We used the observation data to model the CXB and NXB components of the background. The CXB component of background is vignetted by X-optics, but the NXB component is not (Arnaud et al. 2002b). In this analysis we selected of the "flare" events in the observation data, created the surface brightness profile from observation data, used the vignetting function to search the CXB and NXB components of the background by minimising $\chi^2$ in the outer regions. Finally we subtracted the CXB and NXB components from the observation. We obtained cluster emission up to $R_{200}$. After rebinning, the surface brightness profile was fitted with the $\beta$-model, see Fig. 1c. The fit of the cluster profile is given in Table 1.

### 3.2. Summary of image analysis

In our image analysis, the same results were obtained using different backgrounds for subtraction. The surface brightness profile of CL0016+16 was detected up to $R_{200}$, which is important for studying the cluster physics in the outskirts.

In all samples, the $\beta$-model agree well with the surface brightness profiles using the method of double background subtraction. The different results of the fitting $\beta$-model for CL0016+16 are shown in Table 1, obtaining good agreement with other authors.

We obtained worse reduced $\chi^2$ using the background of A. Read and the modelling of background. It may be because the A. Read background has artefacts in the centre of the FOV so the surface brightness profile of the cluster does not fit in the centre well with $\beta$-model. Also in this case, the variation of reduced $\chi^2$ depends on the second background subtraction.

We established that the $\beta$-fit had problems in fitting the core radius, so we fitted the $\beta$-model with the surface brightness profile in the external region and obtained the better values of reduced $\chi^2$. Also, using the template of simulated cluster, we tested the possibility of detecting up to $R_{200}$ with XMM-Newton data (see Appendix A).

With XMM-Newton data, we detected cluster emission of CL0016+16 up to $R_{200}$, it was then so possible to determine the cluster total mass and physical parameters more precisely, to study the physics near the virial radius, and to test self similarity theory. For our spectral analysis, we decided to use the background of Nevalainen, because by using this background we obtained a better result with the $\beta$-model fit.

**Table 1.** The comparison of the $\beta$-model fitting results for the galaxy cluster CL0016+16.

| data source | $\beta$-fit<br>$\beta$ | (0.01–2.5 Mpc)<br>$r_c$(Mpc) | $\chi^2_{\rm reduced}$ | $\beta$-fit by region extern<br>$\beta$ | (0.3–2.5 Mpc)<br>$r_c$(Mpc) | $\chi^2_{\rm reduced}$ |
|---|---|---|---|---|---|---|
| Kotov & Vikhlinin (2005) | 0.76 ± 0.01 | 0.27 ± 0.01 | 1.38 | ... | ... | ... |
| Worrall & Birkinshaw (2003) | 0.70 ± 0.01 | 0.23 ± 0.01 | 1.35 | ... | ... | ... |
| Neumann & Bohringer (1996) | 0.68 ± 0.3 | 0.28 ± 0.14 | 1.02 | ... | ... | ... |
| Using background by A. Read | 0.77 ± 0.01 | 0.31 ± 0.01 | 1.56 | 0.80 ± 0.02 | 0.34 ± 0.02 | 1.35 |
| Using background by J. Nevalainen | 0.76 ± 0.01 | 0.29 ± 0.01 | 1.15 | 0.72 ± 0.01 | 0.29 ± 0.01 | 1.02 |
| Using the modelling<br>of background from observation | 0.76 ± 0.01 | 0.38 ± 0.01 | 1.57 | 0.81 ± 0.02 | 0.38 ± 0.02 | 1.21 |

## 4. Spectral analysis

We needed to study the ICM dynamics of CL0016+16 and to calculate the total mass profile up to $R_{200}$ more precisely using the equilibrium approach. From the spherical brightness emission, CL0016+16 looks like a relaxed cluster without any cool core. On the other hand, CL0016+16 has the companion cluster RX J0018.3+1618 (Worrall & Birkinshaw 2003) and radio halo (Giovannini & Feretti 2000). It is very important to check the equilibrium of this system.

To test the equilibrium, we performed a detailed spectral analysis. The mean temperature, temperature profile, temperature map, temperature in the regions, and the temperature profiles in different directions were obtained. In our spectral analysis, we used three cameras of XMM-Newton, the background from Nevalainen, and the method of double background subtraction by Arnaud et al. (2002b). We fitted the spectra with XSPEC using the redshifted APEC plasma emission model with the absorption $N_{\rm H} = 4 \times 10^{20}$ cm$^{-2}$ and free abundances. In our research, we are more interested in temperature variations; at same time, we fitted temperature with free and fixed abundance (0.18 solar unit, obtained from the best fit of the mean temperature in 6.4′ radius). For each spectrum similar temperatures were obtained in both cases, but sometimes we cannot reliably determine the abundances due to weak statistics.

### 4.1. Mean temperature

The overall MOS1, MOS2, and pn spectra extracted from the event file are shown in Fig. 3. The spectra were corrected for the vignetting and the background. The integration region for the cluster was restricted to 5′ ($R_{200}$), because this region was chosen to test the self similarity theory. The temperature values were estimated for all EPIC cameras MOS1, MOS2, and pn. The best fit gives $kT = 8.81 \pm 0.35$ keV and an abundance of $0.18 \pm 0.05$, the reduced $\chi^2$ is 0.93. We also estimated the mean temperature in a 6.4′ radius, the best fit gives $kT = 8.83 \pm 0.36$ keV with a reduced $\chi^2$ of 0.93 and an abundance of of $0.19 \pm 0.05$ solar units.

### 4.2. Temperature profile

For a more exact determination of the total mass profile, it is better to use the temperature profile. We supposed that CL0016+16 was a relaxed cluster and assumed that the temperature structure of this cluster was spherically symmetric. The spectra were extracted in the five concentric annuli centred on the cluster X-ray emission peak, and we fitted the data as described above. The sizes of the annuli were chosen to optimise the signal-to-noise in each annulus. Note, we fitted spectra for the temperature profile with frozen and free abundances and obtained similar values of the temperature and error bar (see Table 2).

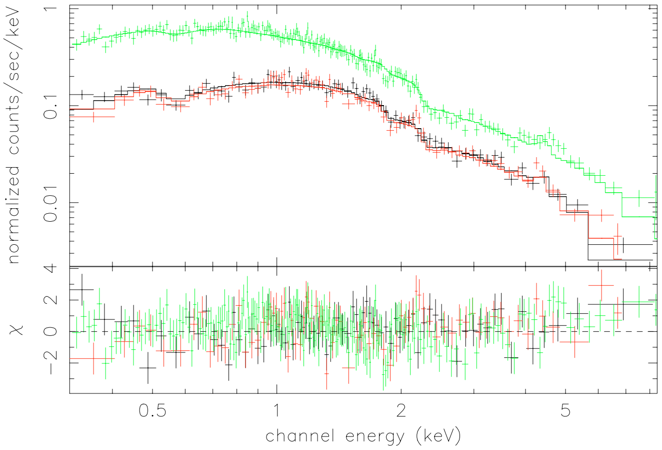

**Fig. 3.** CL0016+16 extracted spectra in the region 5′ from the XMM-Newton data. Black, red, green points are the data from the corresponding EPIC/ MOS1, MOS2, and pn data. The solid lines show the best fit of the isothermal model with $kT = 8.81$ keV and abundance of 0.18 solar units.

We obtained the total temperature profile up to $R_{200}$ (see Fig. 4). The temperature profile is in good agreement with the spectral-fit results of Kotov & Vikhlinin (2005), as seen in the comparison in the figure from our analysis. Note that temperature was detected up to $R_{200}$ and obtained points agree with the function of temperature profile by Kotov & Vikhlinin (2005).

### 4.3. Temperature map

To understand the ICM dynamics of CL0016+16 it is necessary to obtain a temperature map, which is the most accessible measurable indicator of a system equilibrium. The temperature map was obtained by a X-ray wavelet spectral mapping algorithm (XWSM). The spatial temperature variations are coded on different scales in the wavelet space using the Haar wavelet and then denoised by thresholding the wavelet coefficients. For a complete description of the algorithm, see Bourdin et al. (2004).

The CL0016+16 temperature map was computed using three cameras of XMM-Newton. This algorithm fitted the temperature with the APEC plasma emission model. The resulting temperature map shown in Fig. 5 was obtained from a wavelet analysis performed on 5 scales corresponding to a structure of a minimum size of 45″ with a mean temperature of 9 keV and with the same absorption and abundance.

The temperature map was obtained up to 2.5′ (1 Mpc) with a 68% confidence level for all detected structures. The overall appearance of the temperature structure is strongly asymmetric. The maximum of the temperature is 12.52 keV and 8.7 keV in the cold region of the cluster. We observed the maximum of

**Table 2.** The spectral-fit results of the temperature profile with frozen and free abundances for all EPIC cameras.

| annulus<br><br>$r_1$–$r_2$ (′) | $T$(keV)/$\chi^2_{\rm red}$<br>$Z = 0.18\ Z_\odot$<br>mos1+mos2+pn | $T$(keV)/$\chi^2_{\rm red}$<br>free $Z$<br>mos1+mos2+pn | $Z$ ($Z_\odot$)<br><br>mos1+mos2+pn | $T$(keV)/$\chi^2_{\rm red}$<br>free $Z$<br>mos1+mos2 | $T$(keV)/$\chi^2_{\rm red}$<br>free $Z$<br>pn |
|---|---|---|---|---|---|
| 0.0–0.5 | $10.63^{+0.57}_{-0.47}$/0.92 | $10.27^{+048}_{-0.47}$/0.91 | 0.42 ± 0.11 | $11.45^{+1.25}_{-0.95}$/0.88 | $9.58^{+0.62}_{-0.61}$/0.93 |
| 0.5–1.0 | $9.31^{+0.42}_{-0.42}$/1.01 | $9.34^{+0.43}_{-0.43}$/1.01 | 0.15 ± 0.06 | $9.80^{+0.68}_{-0.67}$/1.02 | $9.05^{+0.57}_{-0.56}$/1.00 |
| 1.0–2.0 | $9.17^{+0.51}_{-0.51}$/0.92 | $9.33^{+0.55}_{-0.54}$/0.91 | 0.11 ± 0.07 | $10.23^{+1.19}_{-0.88}$/0.94 | $8.77^{+0.68}_{-0.63}$/0.89 |
| 2.0–4.0 | $6.45^{+0.88}_{-0.62}$/1.03 | $6.32^{+0.75}_{-0.61}$/1.03 | 0.38 ± 0.17 | $8.06^{+1.96}_{-1.36}$/1.03 | $5.19^{+0.88}_{-0.56}$/1.02 |
| 4.0–6.4 | $4.14^{+2.18}_{-1.27}$/0.87 | $4.07^{+2.21}_{-1.30}$/0.85 | ... | $1.99^{+2.43}_{-0.55}$/0.89 | $4.98^{+2.49}_{-2.51}$/0.82 |

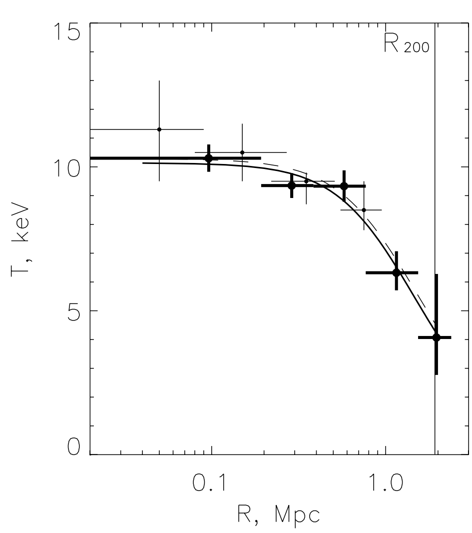

**Fig. 4.** The obtained total temperature profile of CL0016+16. The solid points and line are the obtained temperatures and the fitting of the temperature profile function. The thin points and dotted line are the obtained temperatures and the temperature profile function of Kotov & Vikhlinin (2005).

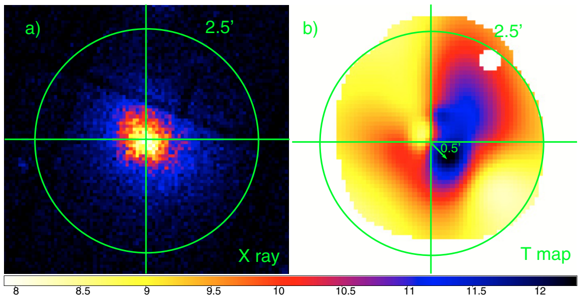

**Fig. 5.** **a)** The X-ray emission from EPIC (MOS1, MOS2, and pn cameras) in the energy band 0.3–4.5 keV. **b)** The temperature map obtained by wavelet algorithm described in Bourdin et al. (2004).

temperature southwest (SW) of the cluster emission centre, and the minimum of temperature northeast (NE) of cluster emission centre. Figure 5 shows the hot regions to the southeast (SE) and to the northwest (NW) and two cold regions in other directions. Note that the maximum of the temperature is not superimposed on the maximum emission. The peak of the temperature is displaced by 0.5′ (190 kpc) from the cluster emission peak.

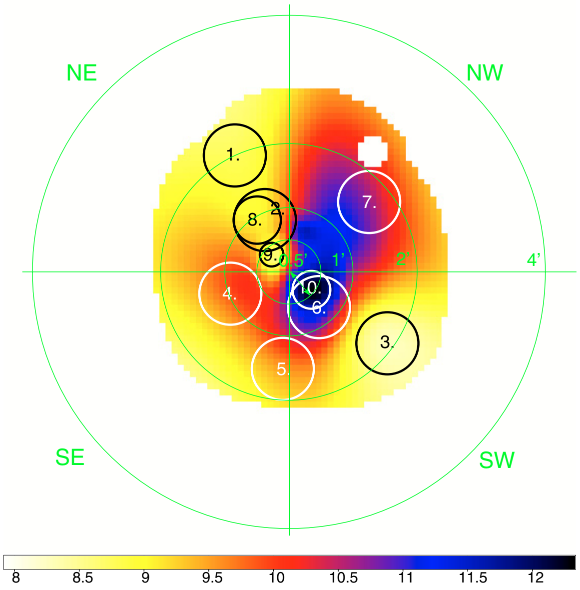

**Fig. 6.** The temperature map with chosen regions and sectors. The white contours illustrate the chosen regions from which spectra were extracted. The regions were defined on the basis of temperature map. The green contours are the sectors chosen, for extracting the spectra for four temperature profiles.

### 4.4. Temperature in selected regions

To check the temperature map obtained with XWSM, we computed the hardness ratio map and observed the same variation in the cluster centre, in the direction of the temperature map elongation from SE to NW. To assess the significance of the temperature variations found in the temperature map, we focused on the spectral fits in specific regions, see Fig. 6. The regions were chosen from the temperature map. These results are shown in Table 3. The temperature obtained for the regions is in good agreement with that from spectral wavelet analysis. More interesting results were obtained for the regions 9, 10, and 3, where the temperatures are $7.81^{+1.01}_{-0.93}$ keV, $12.01^{+1.45}_{-1.34}$ keV, and $6.16^{+1.14}_{-0.87}$ keV, respectively. Regions 9 and 3 are the temperature minima and the region 10 has the highest temperature. The temperature peak does not coincide with the maximum of cluster emission. From our spectral analysis, we established that the temperature variations are approximately 4 keV in the cluster centre. It is important to understand whether these variations in temperature would have any significant effect on the total mass.

**Table 3.** The spectral fits results in the chosen regions, with free abundances. Three EPIC cameras were used.

| Region | $T$(keV)/$\chi^2_{\rm red}$ |
|---|---|
| 1 | $6.60^{+3.14}_{-1.50}$/0.77 |
| 2 | $8.87^{+0.87}_{-0.69}$/0.95 |
| 3 | $6.16^{+1.14}_{-0.87}$/0.69 |
| 4 | $10.28^{+1.64}_{-1.16}$/0.80 |
| 5 | $9.63^{+2.47}_{-1.90}$/1.04 |
| 6 | $11.12^{+1.11}_{-0.74}$/0.90 |
| 7 | $13.77^{+3.99}_{-4.11}$/0.66 |
| 8 | $9.25^{+1.09}_{-1.31}$/1.01 |
| 9 | $7.81^{+1.01}_{-0.93}$/0.77 |
| 10 | $12.01^{+1.45}_{-1.34}$/0.84 |

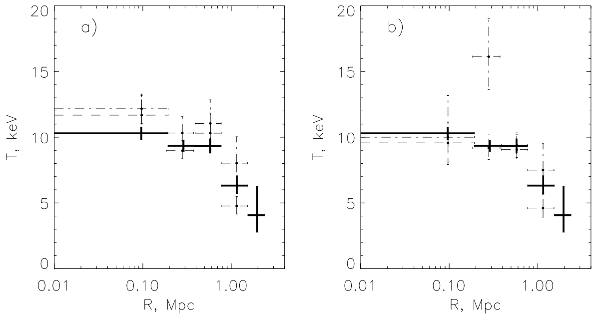

**Fig. 7.** The temperature profiles in different directions. The solid points are the total temperature profile. The dotted points are the obtained temperature profiles from sectors: **a)** the "hot" temperature profiles (the SE and NW directions) **b)** the "cold" temperature profiles (the SW and NE directions) correspondingly. The "cold" temperature profile (SW) in panel **b)** displays a local peak because of the offset of the temperature peak visible in Fig. 6.

### 4.5. Temperature profiles in different directions

To determine the influence of these variations on the total mass, we extracted the temperature profiles in the four different directions. The SE and NW profiles show high temperatures, whereas they are lower in the SW and NE direction. Figure 6 shows the sectors and directions. The reference point of sectors was chosen at the cluster emission centre. The spectra were extracted in each sector up to 4′ (1.54 Mpc). The widths of the annuli were chosen to be similar to that of the total temperature profile. We obtained the temperature profiles in each direction. Figure 7a shows the total temperature profile and two 'hot' temperature profiles. Figure 7b shows the total and "cold" temperature profiles.

We observed the increase in temperature profile compared with the total temperature profile in the SE and NW directions and the decrease in the SW and NE directions. The maximum temperature variations were observed in the cluster centre. We used these temperature profiles to determine the variation in the total mass profiles.

## 5. Mass analysis

To calculate the total mass profile more precisely up to $R_{200}$, we used the temperature and density profiles obtained above assuming hydrostatic equilibrium. To estimate the influence of the temperature variations on the total mass, we computed the total mass obtained with the different temperature profiles presented in Fig. 9 and corresponding $\beta$- parameters. As a result, we performed a surface brightness analysis in each chosen direction and obtained $\beta$-model for each profile (see Table 4).

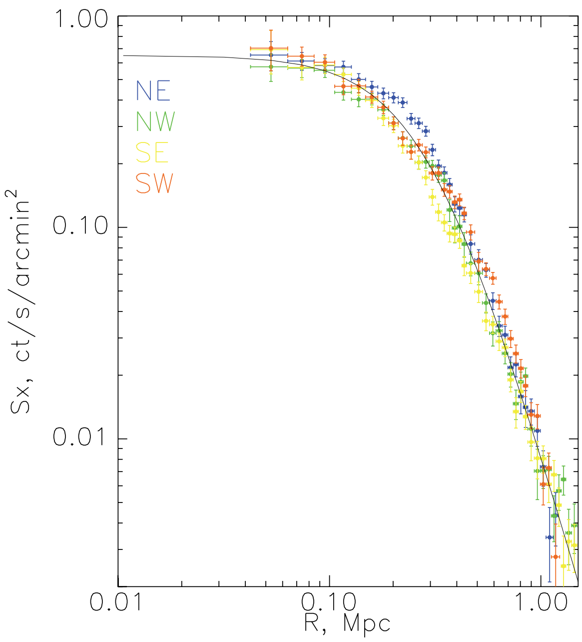

**Fig. 8.** The surface brightness profiles in different directions. The solid line is the best fit of the total radial profile.

**Table 4.** The $\beta$-model fitting results in different directions.

| direction | $\beta$-fit | $r_{\rm c}$(Mpc) | $\chi^2_{\rm reduced}$ |
|---|---|---|---|
| NE | 0.94 ± 0.01 | 0.35 ± 0.01 | 1.05 |
| SE | 0.65 ± 0.01 | 0.18 ± 0.01 | 1.22 |
| NW | 0.72 ± 0.01 | 0.25 ± 0.01 | 1.68 |
| SW | 0.77 ± 0.01 | 0.31 ± 0.02 | 2.3 |

Figure 8 shows the obtained surface brightness profiles. We observed the different perturbation for each direction more significantly in the NW and SW directions from cluster centre to 500 kpc.

### 5.1. Cluster gas mass

Using the electron density, we calculated the total gas density of the ICM and the ICM mass by integrating Eq. (3). We obtained a central electron density of $n_{\rm e0} = (7.85 \pm 0.01) \times 10^{-3}$ cm$^{-3}$ assuming a temperature of 8.85 keV and using the $\beta$-model parameters obtained from the Nevalainen's background subtraction, given in Table 1. The total gas mass is shown in Table 5.

### 5.2. Cluster total mass

Assuming the spherical symmetry and the hydrostatic equilibrium, we calculated the gravitational mass of the cluster CL0016+16.

In the first step of the mass analysis, we assumed that CL0016+16 is isothermal with the temperature of 8.85 keV and took into account error bars on the temperature profile, $\beta$ and $R_{\rm c}$ parameters. The results are presented in Fig. 9. In the second step of the total mass determination, we used the resulting temperature profiles. Using the hydrostatic equilibrium approach, the $\beta$ parameters obtained with the subtraction of Nevalainen's

**Table 5.** The results of CL0016+16 mass analysis using different temperature profiles and cluster parameters.

| parameter | $M(< R_{200})$ ($\times 10^{14}\ M_{\odot}$) | $M(< R_{500})$ ($\times 10^{14}\ M_{\odot}$) |
|---|---|---|
| $M_{\rm gas}$ | 2.24 ± 0.06 | 1.41 ± 0.04 |
| $M_{\rm tot}$, $T = 8.81$ keV | 14.0 ± 0.6 | 8.4 ± 0.3 |
| $M_{\rm tot}$, $T(r)$ | 11.9 ±2.0 | 8.0 ± 1.0 |
| $M_{\rm tot}$, $T(r)NW$ hot | 11.2 ± 2.6 | 8.0 ± 2.1 |
| $M_{\rm tot}$, $T(r)NE$ cold | 11.1 ± 2.4 | 8.1 ± 1.9 |
| $M_{\rm tot}$, $T(r)SE$ hot | 14.0 ± 2.8 | 8.5 ± 1.8 |
| $M_{\rm tot}$, $T(r)SW$ cold | 12.0 ± 2.5 | 9.0 ± 2.0 |
| $VT$ | | |
| $M_{\rm tot}$, $T = 8.85$ keV | 14.42 | |
| $n_{\rm e0}(\times 10^{-3}\ {\rm cm}^{-3})$ | 7.85 ± 0.01 | |
| $f_{\rm gas}$ | 0.16 ± 0.01 | |
| $L_{\rm X}(\times 10^{45}$ erg/s) | 5.1 ± 0.1 | |

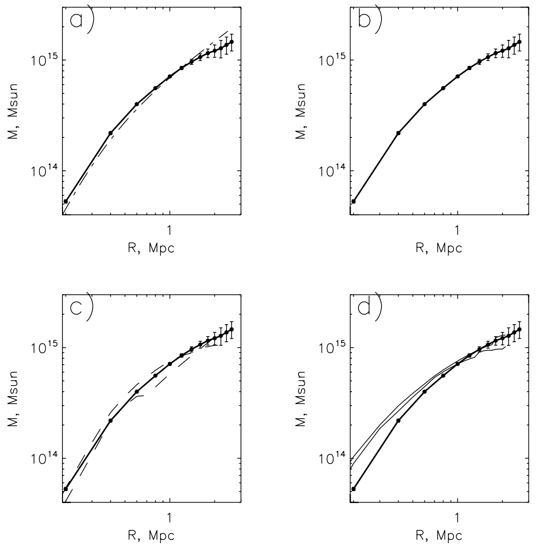

**Fig. 9.** The integrated total mass profile of CL0016+16. **a)** The bold solid line showing the total mass profile was obtained using the total temperature profile. The dot-dashed line is the total mass profile obtained using constant temperature. **b)** The bold solid line is the total mass profile obtained using the total temperature profile. **c)** The solid line is the total mass profile obtained using the "cold" temperature profiles. **d)** The dotted line is the total mass profile obtained using the "hot" temperature profiles.

background and the temperature profile, we calculated the cluster total mass with

$$M_{\rm tot}(< r) = -\frac{k}{G\mu m_{\rm p}} r^2 \left( \frac{{\rm d}T}{{\rm d}r} - 3\beta T \frac{r}{r^2 + r_{\rm c}^2} \right). \tag{4}$$

The mass profile was calculated using the Monte Carlo method, which takes the obtained parameter for the gas density profile and the measured temperature profile as input. The method of Neumann & Bohringer (1997) was used, which allows transformation of the error bars of the temperature profile into error bars of the mass profile.

Table 5 shows the results of our total mass determination. Figure 9 shows the total mass profiles obtained using the constant temperature and assumption temperature profiles. Using a similar approach Kotov & Vikhlinin (2005), we find the same result on the total mass. We extrapolated the temperature profile of Kotov & Vikhlinin (2005) to $R_{200}$, obtaining total mass of $(11.7 \pm 1.7) \times 10^{14}\ M_{\odot}$, which compares very well with the value of $(11.9 \pm 2.0) \times 10^{14}\ M_{\odot}$ using our total temperature profile.

In order to check the influence of temperature variations in the cluster centre on the total mass profiles, we determined four temperature profiles in each direction and the total temperature profile. Using the equilibrium approach and the obtained $\beta$ parameters the total mass was calculated for each temperature profile. The values of the total mass for each temperature profile are shown in the Table 5 up to $R_{200}$ and $R_{500}$. These temperature variations do not significantly affect the total mass, $\Delta M < 20\%$ at the $R_{200}$, in comparison with the total temperature profile. The main contribution to the mass errors in these profiles came from the determination of temperature, which is less constrained in sectors than in the full annuli. It is noticeable that the total mass estimates in sectors are all within $1\sigma$ errors.

The total mass profiles for each temperature profile and total temperature profile are shown in Fig. 9. We found that, in the cluster's central parts, the total mass profiles obtained with the "cold" temperature profiles are lower than the total mass profile obtained with the total temperature. At $R_{200}$ we found the predominance of the total mass in the southern part of cluster.

We also calculated the gas mass fraction of 0.16 ± 0.01, which is simply the ratio of the ICM mass to the total mass.

### 5.3. Total mass from self similarity

Also, the total mass was estimated from the $M - T$ scaling relation using the best fit of the mean temperature in 5′ radius at the cluster redshift and in ΛCDM cosmology. Assuming structural similarity and the virial theorem, we provide a scaling relation between virial mass, radius, and the overall X-ray temperature $Tx$: $M_{VT200}/R_{VT200} \propto T_{\rm X}$. This relation corresponds to a fixed density contrast at redshift $z$ and is derived using the virial theorem: $M_{VT200}/(4/3\pi\rho_{\rm c}R^3_{VT200}) = 200$. This leads to the well-known scaling relation:

$$M_{VT200} \propto (1 + z)^{-3/2} T^{3/2}. \tag{5}$$

To compute the scaling total mass $M_{VT200}$, we used the normalisation factor adapted from the numerical simulations of Bryan & Norman (1998), rescaled at $R_{VT200}$. The result for $M_{VT200}$ is in Table 5. From the virial theorem Eq. (5) and from the hydrostatic equilibrium Eq. (4), we obtained similar results on the total mass.

## 6. Scaling properties

### 6.1. Cluster profile

To study the influence of the cluster properties on the self-similarity we compared the scaling and structural properties of distant "hot" galaxies cluster CL0016+16 with the scaling properties obtained from nearby galaxy clusters.

The self-similarity model is based on the simple assumptions for the cluster formation, derived from the top-hat spherical collapse model (Bryan & Norman 1998). The virialised part of a cluster present at a given redshift corresponds to a fixed density contrast as compared to the critical density of the universe at that redshift. This model makes the definitive predictions in terms of the evolution of cluster properties. We considered the scaled emission measure profiles and the $L_{\rm X} - T$ relation.

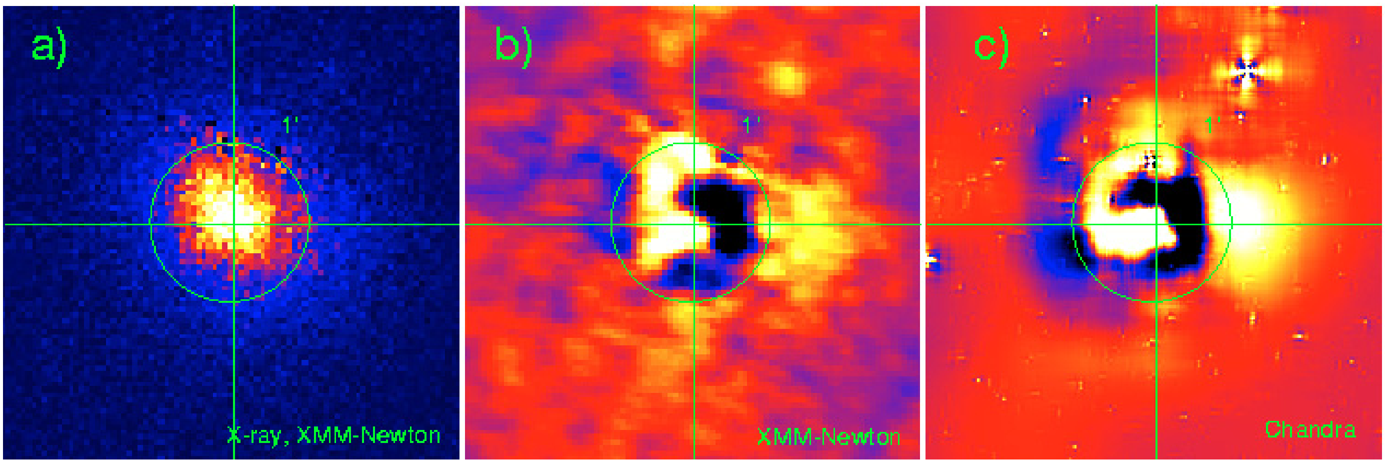

**Fig. 10. a)** The X-ray emission from the XMM-Newton data. **b)** The X-ray residual from the XMM-Newton data in the cluster centre, was obtained with the help of 2D $\beta$-model. **c)** The obtained X-ray residual from the Chandra data.

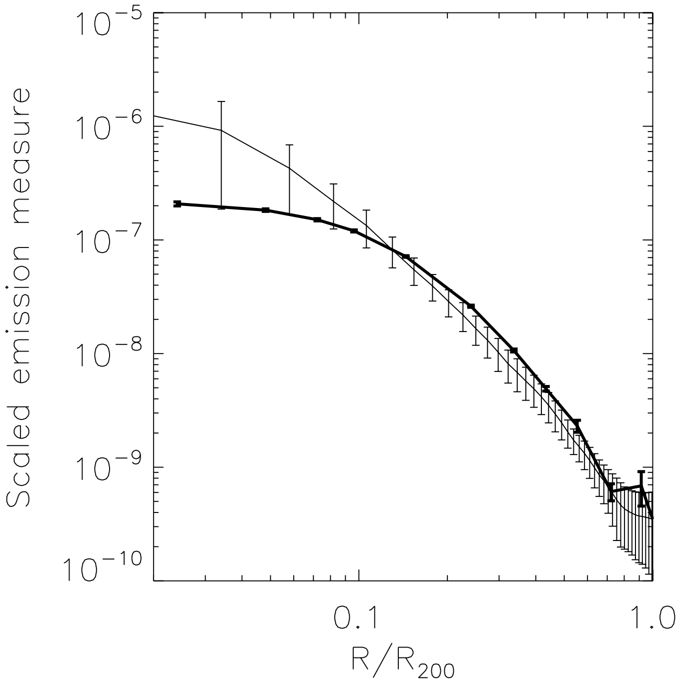

**Fig. 11.** The scaled emission measure (ScEM) profiles. The dotted lines are the ScEM profiles of the nearby clusters. The bold solid line shows the ScEM profile of CL0016+16. The radius is normalised to $R_{200}$.

We used $R_{200}$ for the normalisation on the radius.The self-similarity of cluster implies that the scaled emission measure profile (ScEM) should be identical for all clusters:

$$ScEM(r/R_{200}) = \frac{4\pi(1+z)^4 S(r/R_{200})}{\Lambda(T,z)\sqrt{T}(\sqrt{\Delta_c}E(z))^3}, \tag{6}$$

there, $ScEM(r/R_{200})$ was calculated directly from the observed surface brightness distributions, and $S(r)$ is the obtained surface brightness profile. We applied Eq. (6) to all cluster profiles using the best-fit temperature, corresponding redshift, and the emissivity $\Lambda(T,z)$.

Using $\Lambda$CDM cosmology, we compared the ScEM profile of CL0016+16 observed with XMM-Newton in the 0.3–2 keV band with the ScEM profiles of twelve nearby galaxy clusters observed with ROSAT in the 0.5–2 keV band (Neumann 2005). The nearby galaxy clusters were obtained in the temperature range ($1.7 < kT < 8.5$) keV (but most of them in the 5–6 keV range). The relative error in the calibration of XMM/EPIC and ROSAT/PSPC can be neglected (Arnaud et al. 2002b). Figure 11 shows the average ScEM profiles of nearby galaxy clusters and the ScEM profile from CL0016+16.

We confirm that, in the cluster centre, the ScEM profiles show a large dispersion, which can commonly be explained by the non-gravitational processes. The ScEM profile of CL0016+16 is lower in the centre in comparison with the average ScEM profile, which is the consequence of the absence of a cooling core. In outer regions ($r > 0.2R_{200}$), the ScEM profile of CL0016+16 is higher than the average ScEM profile of nearby galaxy clusters. We compared the total emission from CL0016+16 and from the nearby galaxy clusters at the radii $0.2R_{200} > r > R_{200}$. The total scaled emission of CL0016+16 is stronger by a factor of 1.6 than the total emission from nearby galaxy clusters. Finally, these results can be explained by the cluster properties of CL0016+16, in particular by the absence of cooling core and high luminosity, due to a merger activity.

### 6.2. $L_X$–$T$ relation

We tested the scaling $L_X - T$ relation for a distant luminous galaxy cluster with a possibility of merger. We computed the bolometric luminosity $L_X$ within $R_{200}$ (see Table 5) and obtained the count rate in the 0.3–4.5 keV. The integrated surface brightness profile was converted to bolometric luminosity using the best-fit $\beta$-model from Nevalainen's background subtraction and the instrumental response. The error in $L_X$ includes the statistical errors on the count rate and temperature. We tested the $L_X$–$T$ using a scaling relation from Arnaud & Evrard (1999), $L_X \propto T^{2.88}$. This relation was obtained for sample clusters with weak or absent cooling flow signatures, so it can be used for CL0016+16. Taking the simple mean temperature, scaling relation by Arnaud & Evrard (1999) for our cosmology, and normalisation evolution factor to our distant cluster, we found that CL0016+16 is more luminous by a factor of 2.1 for this temperature. These results confirmed the possibility of a merger in the maximum core collapse for CL0016+16, because the numerical simulation (Randall et al. 2002) suggests that the effect of the merger is to boost the luminosity and the temperature for a short time, and this can have an obvious effect on the scaling relation.

### 6.3. 2D $\beta$-analysis, X-ray residuals

To better understand the status of the cluster dynamics in the centre, we performed a two-dimensional fit to the cluster surface brightness, using a modified $\beta$-model that allows for two different core radii along the two principal axes of cluster image ellipse. We fitted the surface brightness distribution of CL0016+16 obtained from XMM-Newton data with a 2D $\beta$-model and quantified the deviation from this model.

For the XMM-Newton data, we used three cameras, with the modelling and subtraction of background from the image (same method were used in Sect. 3.1.3) and with point sources and gap corrections. To confirm XMM/Epic 2D $\beta$ analysis, we also used the Chandra data to compare the residuals at a better spatial resolution. We are confident of the reality of these residuals since we found very similar results with XMM/EPIC and Chandra/ACIS. A reduced, cleaned ACIS event list was downloaded directly from the Chandra X-ray Center (CXC). The analysis was performed with CIAO software. The images were smoothed with a Gaussian filter before fitting. We fitted 2D $\beta$-model in the region $2'$ (0.8 Mpc $\approx R_{500}$). The best-fit parameters are listed in Table 6. All parameters were assumed free in the fit.

The residuals are shown in the Fig. 10. We obtained very similar results from the XMM-Newton and Chandra data. But we obtained a different core radius because we used a different satellite with a different PSF. Notice that we do not take the PSF into account, which explains the difference in the core radii. Two very similar residual maps established the perturbations at the centre over at least a $1'$ radius (0.4 Mpc). In both cases, the perturbations in the cluster centre were observed with 20% deviation from the maximum cluster emission.

After radial projection, we obtained a rather good $\beta$ fit for the total surface brightness profile, but we observed perturbations in 2D. At first glance, CL0016+16 looks rather homogeneous in brightness and not in temperature. Now, after the 2D $\beta$ subtraction, we enhanced the brightness structures in the inner core. We observed perturbations in the temperature and in the surface brightness distributions in the cluster centre. Quantitatively, these 2D $\beta$-model residuals do not lead to strong variations in density profiles (hence in the mass estimate in the HE scheme), but they are important for qualifying the relaxation status of the inner core of CL0016+16 and thus the limit of the hydrostatic equilibrium hypothesis.

If CL0016 is in the maximum core collapse phase, it will present very similar residuals as observed in numerical simulations around this phase. See, for example, Fig. 4 in Ricker & Sarazin (2001), where they present a 1-to-1 mass ratio collision with a high-impact parameter. Following that scheme, we can estimate the time since core collapse passage by more precise comparison with these simulations. CL0016+16 is 2 times too luminous than the simulation found for a cluster at 0.01 Gyr around its maximum core collapse (see Fig. 5 in Ricker & Sarazin 2001).

## 7. Discussion

In previous works, CL0016+16 was always considered as a very massive *relaxed* cluster. In our present analysis, we find the strong evidence that, at least in the centre, the cluster is not relaxed. From the weakest to the strongests argument favouring the merger scenario, we found:

- CL0016+16 was about a factor of 2 too bright, when compared to the expected luminosity of the $L_X - T$ relation.
- We detected similar significant residuals after subtraction of a 2D $\beta$-model fit using both XMM-Newton and Chandra observations, especially in the inner region ($r < 1' \approx 400$ kpc). Notice that the X-ray maximum was not in the centre of the D $\beta$-model fit.
- The temperature map of the $2.5'$ region (i.e. up to 1 Mpc) clearly looks like an equal mass merger at first maximum core collapse showing significant azimuthal variations.

**Table 6.** The best-fitting results of the 2D $\beta$-model, from the XMM-Newton and Chandra data

| Parameter | Best-fitting<br>XMM | Chandra |
|---|---|---|
| $R_{c1}$(Mpc) | 0.291 | 0.237 |
| $R_{c2}$(Mpc) | 0.364 | 0.295 |
| $\beta$ | 0.79 | 0.79 |
| PA | 2.24 | 2.33 |
| RA | 00:18:33 | 00:18:33 |
| Dec | 16:26:06 | 16:26:11 |

In addition, CL0016+16 is also well known as hosting a strong radio halo, which also argues in favour of a merging cluster (Giovannini & Feretti 2000). Also, we obtained a high-velocity distribution of galaxies for this cluster. Using NED data, we obtained $\sigma_v = 1800$ km s$^{-1}$ for the 150 galaxies at CL0016+16 redshift. The maximum of this map is offset by $0.4'$ (141 kpc) with the X-ray one. We tried to quantify the impact this could have on the total mass estimation and found that, depending on the adopted temperature profiles (but always in the framework of hydrostatic equilibrium), the total mass may vary by something like 20%, which is much greater than the quoted error around 5%. (The errors in the temperature profile is the main contributor to this error budget.)

The main results of our detailed analysis of the galaxy cluster CL0016+16 from the XMM-Newton data can be summarised as follows. We performed detailed image and spectral analyses of the XMM-Newton data using three different backgrounds. In all cases we detected the cluster emission up to $R_{200}$ with the XMM-Newton data. Also using the template of simulated cluster we checked the possibility of detection with XMM-Newton data up to $R_{200}$ (see Appendix A). All these surface brightness profiles give a good fit with the $\beta$-model.

We studied the dynamics of CL0016+16 from the detailed spectral analysis. The global temperature estimated in $5'$ is 8.81 keV, but the spectral study shows that this cluster is not isothermal. We obtained the temperature profile, which decreases in the outer regions, and our results are in a good agreement with results from Kotov & Vikhlinin (2005). The temperature map shows the asymmetry in the radius $1'$, and the temperature maximum ($T = 12.0 \pm 1.5$ keV) is not superposed on the central X-ray cluster emission and is located in SW direction; also we observed the "cold" regions ($T = 6.2 \pm 1.2$ keV) to the SW. To study the dynamics of CL0016+16 more precisely, we chose several regions using the temperature map. We extracted temperature in the regions and found no spherical symmetry in temperature and the presence of the "cold" and "hot" regions in the cluster centre.

We tested the influence of the temperature variations on the cluster total mass using the obtained "cold" and "hot" temperature profiles. We calculated the total mass within $R_{200}$ and $R_{500}$, but the temperature variations do not significantly impact on the total mass, $\Delta M < 20\%$ at $R_{200}$. But the temperature variations in the centre mainly influence the inner part of total mass profile.

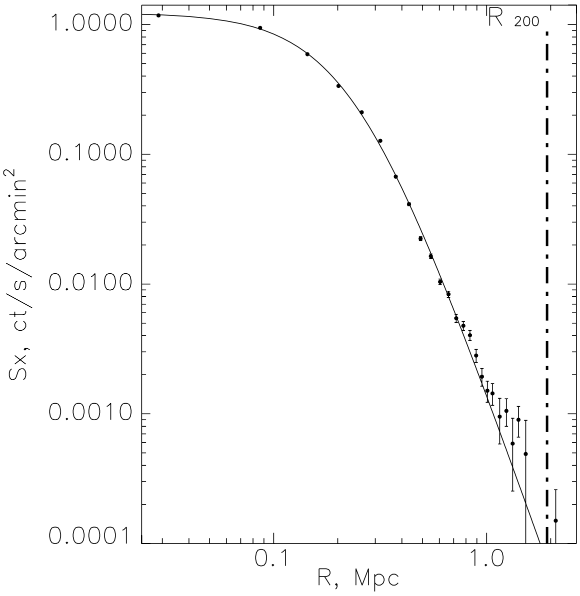

**Fig. A.1.** The surface brightness profile for a similar cluster to CL0016+16 obtained from the Hydro N-body cosmology simulations.

To better understand the possible dynamics in the cluster centre, we calculated a 2D $\beta$-model from XMM-Newton and Chandra observations. The same residuals were obtained in the cluster centre, which may be an indication of merging.

We tested CL0016+16 on the self-similarity theory. The ScEM of distant galaxy cluster CL0016+16 is higher than the mean ScEM profile of nearby clusters in external regions. In the centre we saw larger dispersion, which can be explained by non-gravitational processes. We tested $L_X - T$ relation using scaling relation from Arnaud & Evrard (1999) and concluded that CL0016+16 is more luminous by a factor of 2 for this temperature. It is also the argument for maximum core collapse in CL0016+16.

*Acknowledgements.* We would like to thank Dominique Aubert for performing the numerical simulations of Cluster 6 and making the simulated data available for us to test the possibility of detection up to $R_{200}$ with XMM-Newton. We also would like to thank Herve Bourdin for making the XWSM code available to us.

## Appendix A: Possibility of detection up to $R_{200}$ with XMM-Newton

To check the possibility of the cluster emission detection up to $R_{200}$ with XMM-Newton data, we decided to treat the template of a similar cluster from the Hydro $N$-body cosmology simulation, code RAMSES (Teyssier 2002).

The main idea for using numerical simulation was only to check the ability of XMM/EPIC to detect such a massive cluster at this redshift up to its virial radius, taking all the observational effects into account as precisely as possible, in particular, the relationship between the background, the instrumental response, and the hot temperature of this cluster. The scaling applied to Cluster 6 directly follows the M-T relation and allow properly study of the instrumental effect and limits.

We want to obtain similar cluster using the adaptive mesh-refinement 3-D hydrodynamical cosmology simulation of structure formation (Teyssier 2002). Cluster 6 was formed at a temperature of 3.4 keV.

We used the self-similarity theory to scale the Cluster 6 to CL0016+16, in particular its temperature and mass, without changing the radial profile (below, we refer to this cluster as a simulated cluster). To obtain the cluster emission from the simulation, we created the photons using the Monte Carlo approach. We calculated emission measure per cell using the cell size, density, and the solid angle that depends on the chosen cosmology (Bourdin et al. 2004).

The photons were obtained from cosmology simulation for the simulated cluster. We convolved these photons with the XMM-Newton response. In our analysis we took into account the PSF effect, vignetting correction function, and mask of CCD cameras (gap) and then added the randomly selected events from the background data of A. Read. The same data reduction was performed as for CL0016+16. Figure 4 shows the resulting surface brightness profile for the simulated cluster. Notice that Cluster 6 is cuspier than CL0016+16, its $\beta$-model parameters are $\beta = 0.99$, and the core radius $r_c = 0.24$ Mpc. We still detect the emission of a simulated cluster up to $R_{200}$ but with less significance, see Fig. A.1. This is a rather robust confirmation that XMM-Newton can detect the bright cluster emission up to $R_{200}$.

## References

Arnaud, M., & Evrard, E. A. 1999, MNRAS, 305, 631
Arnaud, M., Neumann, D. M., Aghanim, N., et al. 2001, A&A, 365, L80
Arnaud, M., Aghanim, N., & Neumann, D. M. 2002a, A&A, 389, 1
Arnaud, M., Majerovwicz, S., Lumb D., et al. 2002b, A&A, 390, 27
Baumgartner, W. H., Loewenstein, M., Horner, D. J., & Mushotzky, R. F. 2005, ApJ, 620, 680
Birkinshaw, M., Gull, S. F., & Moffet, A. T. 1981, ApJ, 251, L69
Belsole E., Pratt, G. W., Sauvageot, J. L., & Bourdin H. 2004, A&A, 415, 821
Belsole, E., Sauvageot, J. L., Pratt, G. W., & Bourdin H. 2005, A&A, 430, 385
Bourdin, H., Sauvageot, J. L., Slezak, E., et al. 2004, A&A, 414, 429
Bonamente, M., Joy, M., La Roque, S., et al. 2006, ApJ, 647, 25
Bryan, G. L., & Norman M. L. 1998, A&A, 495, 80
Cavaliere, A., & Fusco-Femiano, R. 1976, A&A, 49, 137
Clowe, D., Luppino, G. A., Kaiser, N., & Cioia, M. I. 2000, ApJ, 539, 540
Comerford, J. M., Menegnetti, M., Bartelmann, M., & Schirmer, M. 2006, ApJ, 642, 39
Cole, S., & Lacey, C. 1996, MNRAS, 281, 716
Evrard, A. E., Metzler, C. A., & Navarro, J. F. 1996, ApJ, 469, 494
Giovannini, G., & Feretti, L. 2000, New Astronomy, 5, 335
Hughes, J. P., & Birkinshaw, M. 1998, ApJ, 497, 645
Kotov, O., & Vikhlinin, A. 2005, ApJ, 633, 781
Majerowicz, S., Neumann D., & Reiprich, T. 2002, A&A, 394, 77
Majerowicz, S., Neumann, D. M., Romer, A. K., et al. 2004, A&A, 444, 673
Neumann, D. 2005, A&A, 439, 465
Neumann, D. M., & Bohringer H. 1997, MNRAS, 289, 123
Neumann, D., & Arnaud M. 1999, A&A, 348, 711
Nevalainen, J., Markevitch, M., & Lumb, D. 2005, ApJ, 629, 172
Randall, S. W., Sarazin, G. L., & Ricker, P. M. 2002, ApJ, 577, 579
Read, A., & Ponman, T. 2003, A&A, 409, 395
Ricker, P. M., & Sarazin, G. L. 2001, ApJ, 561, 621
Sauvageot, J. L., Belsole, E., & Pratt, G. W. 2005, A&A, 444, 673
Vikhlinin, A., Forman W., & Jones, C. 1999, ApJ, 525, 47
Tanaka, M., Kodama,T., Arimoto, N., et al. 2005, MNRAS, 362, 268
Teyssier, R. 2002, A&A 385, 337
Worrall, D. M., & Birkinshaw, M. 2003, MNRAS, 340, 1261